Supporting Information for:

Monolithic Photoelectrochemical Device for Direct Water Splitting with 19% Efficiency

Wen-Hui Cheng [†,‡], *Matthias H. Richter* [‡,§], *Matthias M. May* [*,||,⊥,#], *Jens Ohlmann* [▽],

David Lackner [▽], *Frank Dimroth* [▽], *Thomas Hannappel* [*,#],

Harry A. Atwater [*,†,‡], *Hans-Joachim Lewerenz* [‡,○]

†Department of Applied Physics and Material Science, California Institute of Technology, Pasadena, California 91125, United States

‡Joint Center for Artificial Photosynthesis, California Institute of Technology, Pasadena, California 91125, United States

§Division of Chemistry and Chemical Engineering, California Institute of Technology, Pasadena, California 91125, United States

|| Department of Chemistry, University of Cambridge, CB2 1EW Cambridge, United Kingdom

⊥ Helmholtz-Zentrum Berlin für Materialien und Energie GmbH, Institute for Solar Fuels, D-14109 Berlin, Germany

#Department of Physics, Technische Universität Ilmenau, D-98693 Ilmenau, Germany

▽Fraunhofer Institute for Solar Energy Systems ISE, D-79110 Freiburg, Germany

○Division of Engineering and Applied Science, California Institute of Technology, Pasadena, California 91125, United States

Corresponding Author

*E-mail: haa@caltech.edu; thomas.hannappel@tu-ilmenau.de; matthias.may@physik.hu-berlin.de

Section S1. Device fabrication

Tandem light-absorber photoelectrode synthesis

The dual-junction light absorber ($Ga_{0.41}In_{0.59}P/Ga_{0.89}In_{0.11}As$ with 1.78 eV and 1.26 eV) was grown by metal-organic vapor phase epitaxy in an Aixtron 2800-G4-TM reactor [1,2] on a 4'' p-GaAs (100) wafer with 6° offcut to [011] using a GaInAs metamorphic step-graded buffer layer to overcome the difference in lattice-constant between the substrate and the solar cell layers. The threading dislocation density after the metamorphic buffer is below $1x10^6$ cm^{-2}. Further details (layer composition and thickness) is given in reference [1,2].

Photocathode fabrication

The native oxide on the back of the GaAs substrate was removed prior to metal ohmic contact deposition by (1) rinsing in acetone; (2) isopropanol; (3) 30 sec NH_4OH (10 %); (4) H_2O:N_2 and (5) drying in N_2. Immediately afterwards 70 nm Pd, 70 nm Ti and 200 nm Au were deposited by electron beam evaporation followed by rapid thermal annealing at 400 °C for 60 s under N_2 atmosphere [3].

Prior to the TiO_2 layer deposition, the front GaAs/GaInAs cap layer was removed in a chemical etch bath. The sample was (1) degreased by 15 s rinsing in 2-propanol, (2) 15 s in H_2O:N_2 followed by (3) a 60 s etch step in 25 % NH_4OH:30 % H_2O_2:H_2O (1:1:10), finishing with (4) a 20 s rinse in H_2O:N_2 and (5) drying under N_2 (Fig. S1, step 1). Directly afterwards (a desiccator was used for sample transfer between systems), TiO_2 was deposited by atomic layer deposition (ALD) in an Ultratech Fiji F200/G2 ALD system using a titanium tetraisopropoxide (TTiP) precursor (STREM Chemical Inc.) and water as the oxidizer. The deposition temperature was set to 250 °C and a total of 1500 ALD cycles were carried out (Fig. S1, step 2). No high temperature post annealing is required.

Note that the edge of the sample has been carefully removed to prevent shunting of the front and back surfaces. Ag paste was applied to attach an ohmic contact to a coiled, tin-plated Cu wire which was then threaded through a glass tube. The sample was encapsulated and sealed to the glass tube using black epoxy (Electrolube ER2162).

The Rh catalyst was photoeletrodeposited (Fig. S1, step 3) in an aqueous solution of 0.5 mM Rh(III) chloride trihydrate (99.98%, Sigma Aldrich) + 0.5 M KCl (99.5%, Alfa Aesar) at +0.3 V vs. an SCE reference electrode under pulsed illumination. White light was provided by an Oriel Instruments Solar Simulator using a 1000 W Mercury-Xenon arc lamp. The frequency of the stroboscopic illumination resulted from the optical chopper frequency and the double structure of the chopper wheel. The resulting current profile is shown as an inset in Fig. 1c.

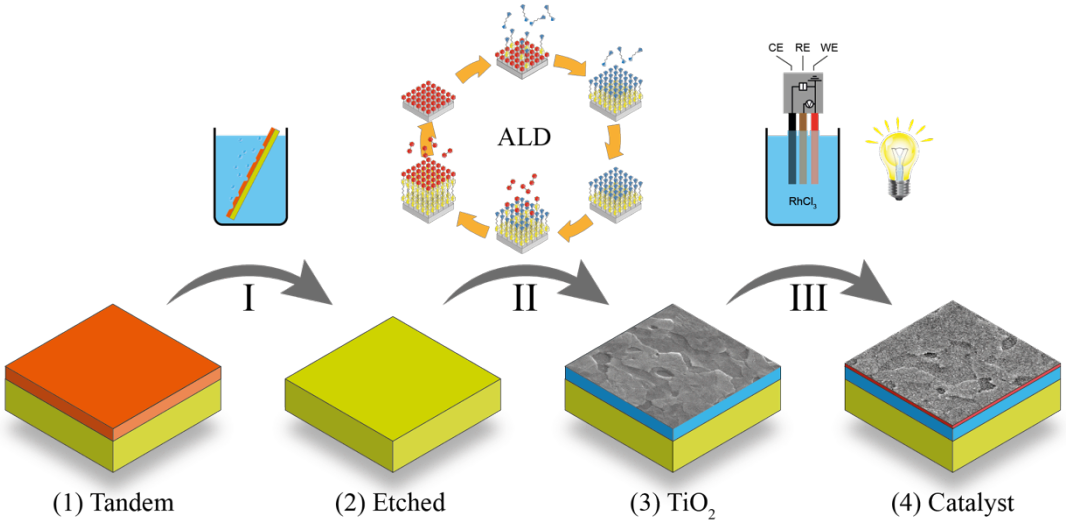

Figure S1. Process flow for preparing the PEC device: (I) Chemical etching of the GaAs/GaInAs cap layer stopping at the AlInP window layer. (II) Deposition of the TiO_2 protection and antireflection coating with ALD. (III) Photoelectrochemical deposition of a closed layer of Rh nanoparticles onto the tandem.

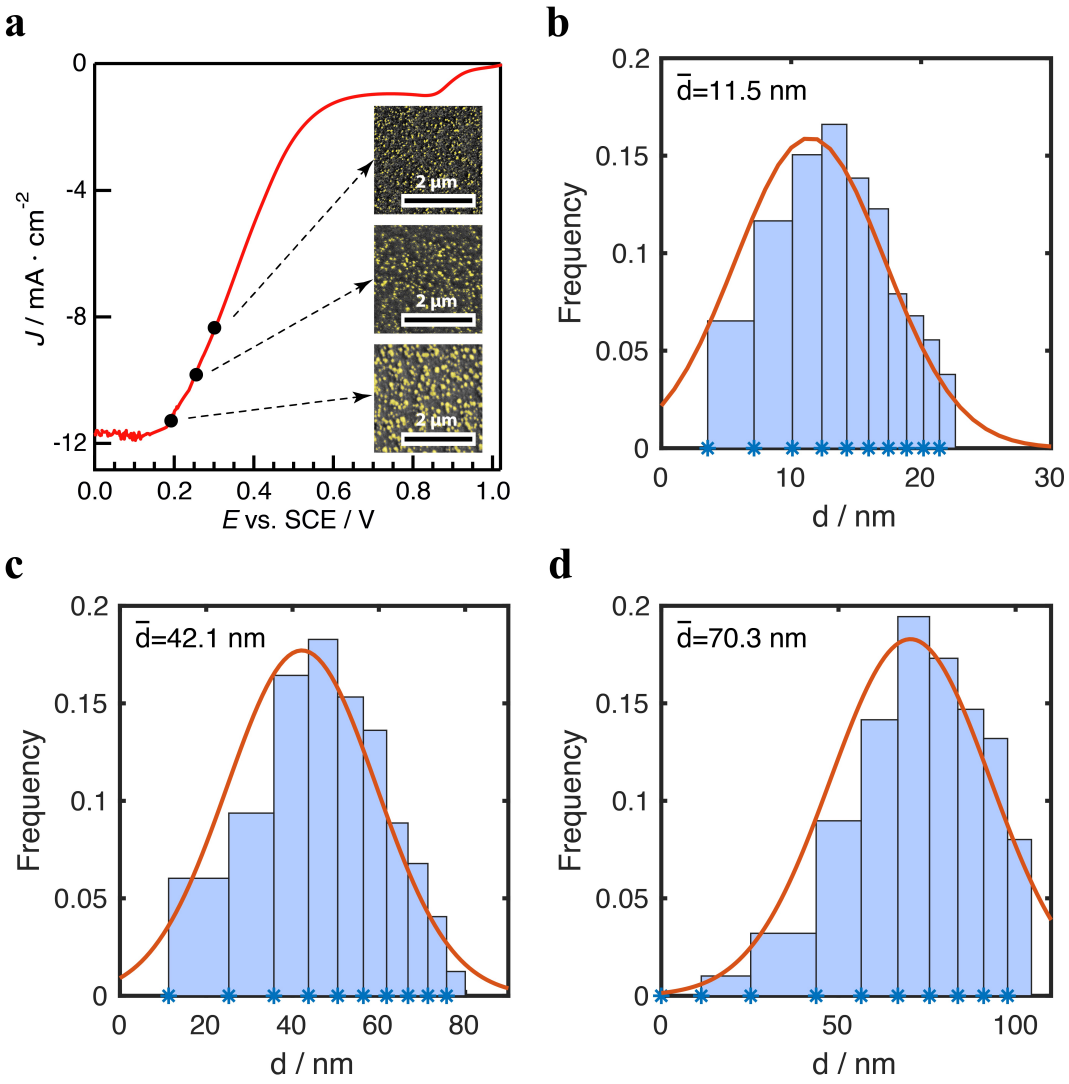

Figure S2. (a) Fine control of particle size d ranging from 10 nm to 100 nm is achievable by appropriate adjustment of the potential during catalyst electrochemical deposition. The three images on the right inset are SEM images with scale bar 2 μm. (b-d) Particle size histograms correspond to each SEM image depicted from top to bottom in (a) with the most frequent particle size indicated by $\bar{d}$.

Counter electrode fabrication

Counter electrodes were prepared by sputtering ruthenium for 60 min on titanium foil (0.125 mm, 98 %, Sigma Aldrich) using an AJA sputtering system with a forward RF power of 200 W, 5 mTorr Ar atmosphere and a base pressure of $2x10^{-8}$ mTorr. The as prepared electrodes were cut into 1 cm^2 pieces, attached with Ag paste to a tin-plated Cu wire which was then threaded through a glass tube. The counter electrode sample was encapsulated and sealed to the glass tube using black epoxy (Electrolube ER2162).

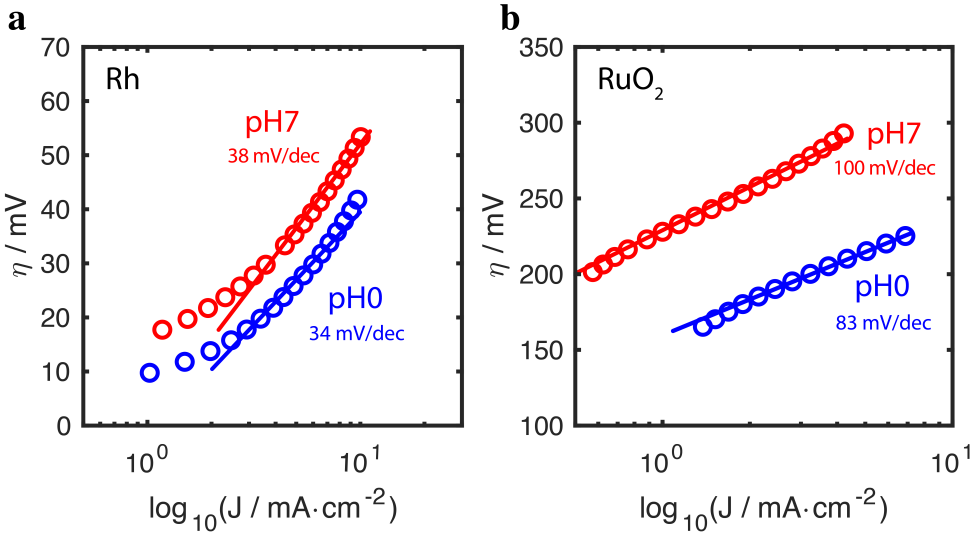

Figure S3. Tafel plots of (a) Rh and (b) RuO_2 catalysts under pH 0 and pH 7 conditions. The Tafel slopes are 34, 38, 83 and 100 $mV \cdot dec^{-1}$ for Rh-pH_0, Rh-pH_7, RuO_2-pH0, and RuO_2-pH7 respectively.

Section S2. Materials characterization techniques

Optical and surface analyses

Optical measurements were performed to obtain reflectivity spectra for different surface layer stacks in air. A Cary 5000 UV/vis/NIR with integrating sphere that include diffuse reflectivity measurement was used. For surface topography studies, a Bruker Dimension Icon AFM in Peakforce mode was used. Scanning electron microscopy images were obtained with a FEI Nova NanoSEM 450 microscope.

Photoelectron spectroscopy

XPS measurements were performed using a Kratos Axis Ultra and Surface Science M-Probe system with a base pressure of $< 1x10^{-9}$ mTorr. A monochromatic AlKa (hK = 1486.69 eV) source with a power of 150 W was used for all measurements. He I ultra violet photoelectron spectroscopy (UPS) was performed on the Kratos Axis Ultra system using a Helium gas discharge lamp.

Section S3. TiO_2 characterization

Amorphous defective TiO_2 coatings have been commonly applied using ALD with Tetrakis(dimethylamino)titanium (TDMAT) precursors to yield protected photoanodes, a concept designed to facilitate transport of holes through a defect band in the TiO_2 [4,5]. However, the dominant process that limits the photoelectrochemical performance of high-quality semiconductors is not transport but interface recombination. Thus, we instead utilize a defect band free, microcrystalline anatase phase TiO_2 coating formed by ALD with titanium tetraisopropoxide (TTiP) precursors as an electron-selective contact to protect the surface of photocathode from photocorrosion.

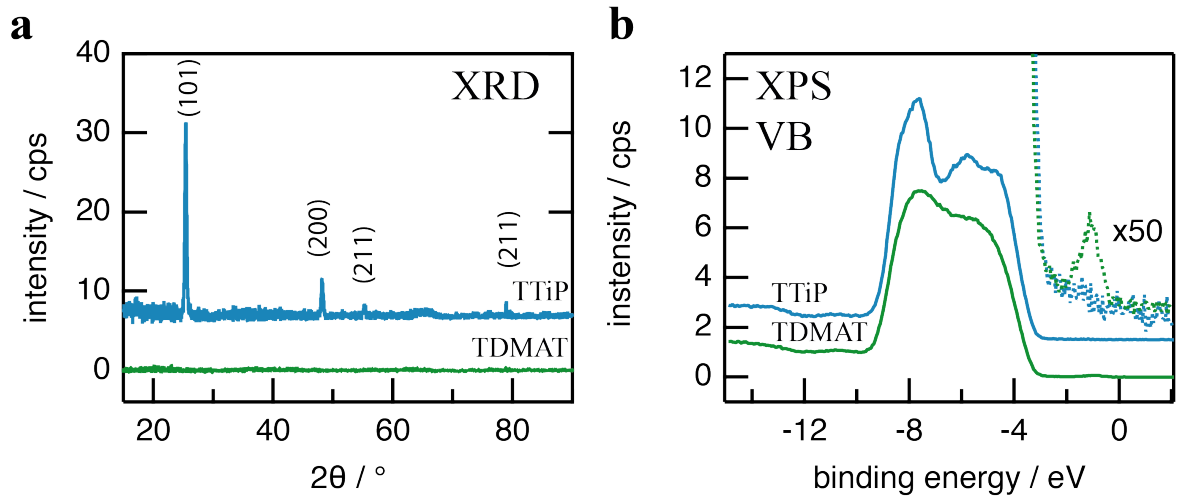

Figure S4. (a) X-ray diffraction data of ALD deposited TiO_2 from TTiP or TDMAT precursor. The TTiP TiO_2 shows anatase crystalline phase while the TDMAT TiO_2 is amorphous. (b) XPS valance band spectra of TTiP and TDMAT TiO_2. A defect band in TDMAT TiO_2 can be observed at -1 eV which facilitates hole transport in photoanodes [4]. Instead, TTiP TiO_2 exhibits an XPS spectrum without a defect band and would be more suited to prevent recombination in photocathodes.

Section S4. Surface layer band alignment

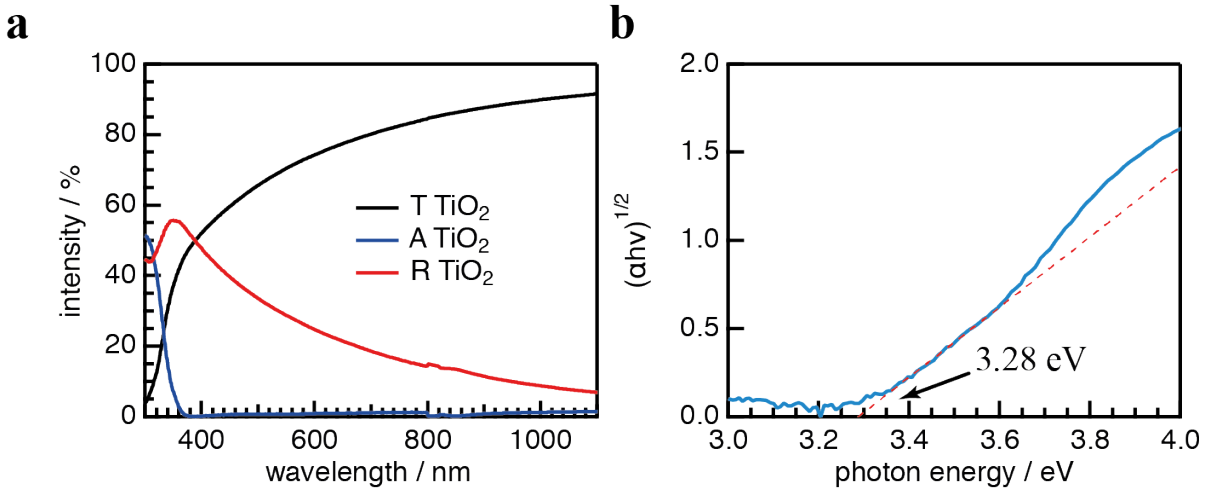

Figure S5. (a) Optical properties (A: absorption, T: transmission, R: reflection) of TiO_2 (TTiP ALD) in air. (b) Tauc plot of ALD grown TiO_2. The intersection with the horizontal axis indicates an indirect optical gap around 3.3 eV. Together with the 4.5 eV work function from Fig. S6a and the 3.2 eV Fermi level to valence band edge difference obtained by the valance band spectrum of TTiP TiO_2 in Fig. S4b, we can obtain the full band diagram of TiO_2.

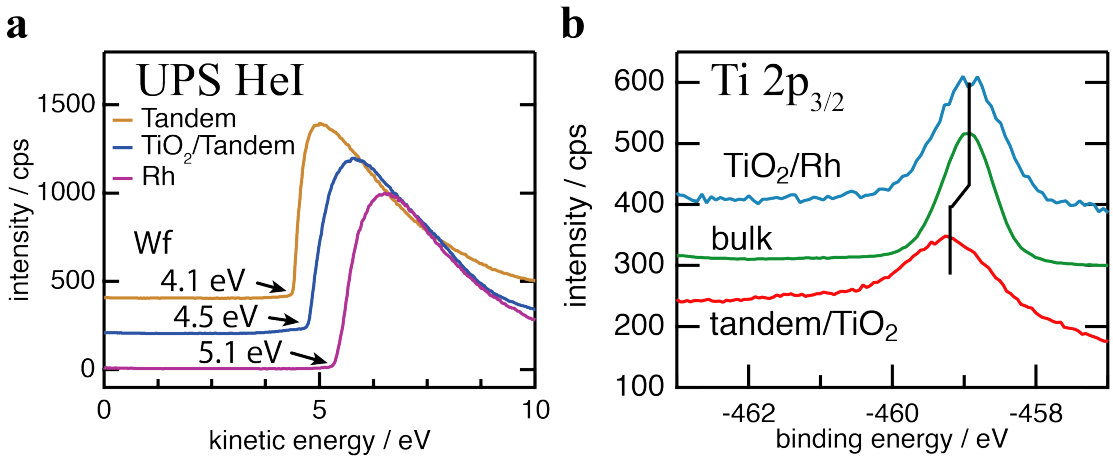

Figure S6. (a) Work function measurements by UPS for the tandem, for TiO_2 on the tandem and for Rh metal. The increase of work function from 4.1 eV to 4.5 eV was observed after applying TiO_2 protection layer on tandem. The Rh metal spectrum is measured on the foil as reference instead of the photoelectrochemical deposited nanoparticles. (b) Core level shift of Ti $2p_{3/2}$ indicating ~0.3 eV downward band bending at the tandem/TiO_2 interface and nearly no band bending at the TiO_2/Rh interface. The tandem/TiO_2 sample was made with 40 ALD cycles TiO_2 on top of the tandem. The Rh has originally high metal work function of 5.1 eV but does not create band bending at the junction with TiO_2. This can be explained by the pinch-off effect when the metal NPs are small enough that the Fermi level would directly attach to the semiconductor Fermi level without creating a barrier [6].

The final surface band alignment as displayed in Fig. S7 can be obtained after aligning the Fermi level of the solid state device to the hydrogen evolution potential (HER) at 4.6 eV. Due to the higher work function of 4.5 eV for TiO_2 than 4.1 eV for the tandem, a lower barrier from 0.5 eV to 0.1 eV for hydrogen evolution (HER) will be expected.

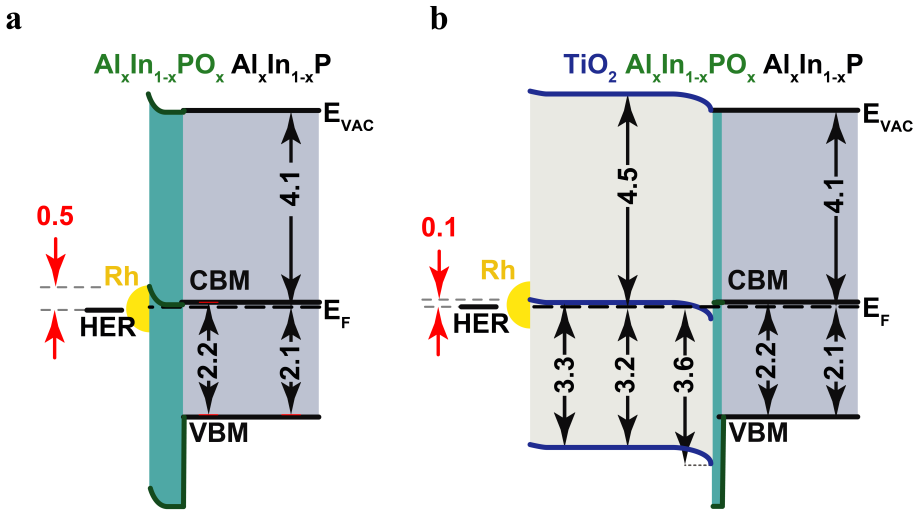

Figure S7. Surface band alignment of the electrolyte interface layers (a) without and (b) with TiO_2 are shown as a comparison. The values are shown as energy with unit of eV.

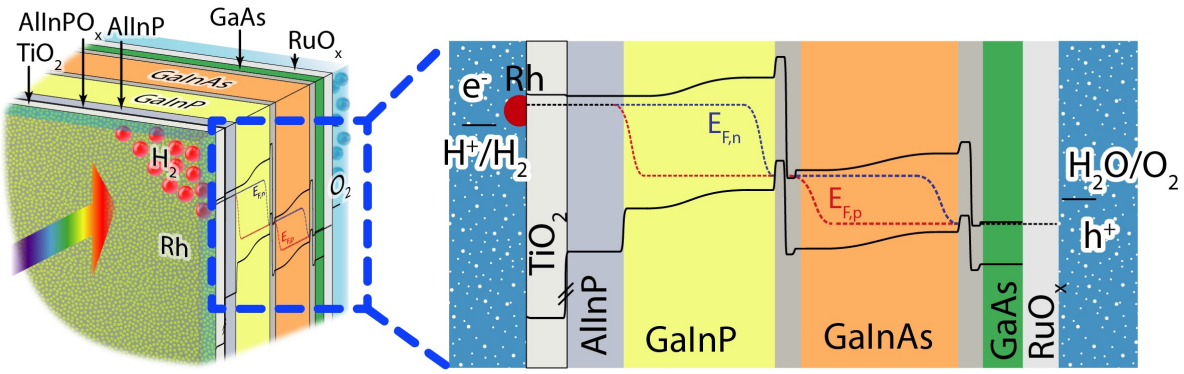

Figure S8. Illustration of the photoelectrochemical water splitting device structure. Band alignment at the operation point is depicted on the side and zoomed in to gain the visibility.

Section S5. Absorption enhancement by TiO_2

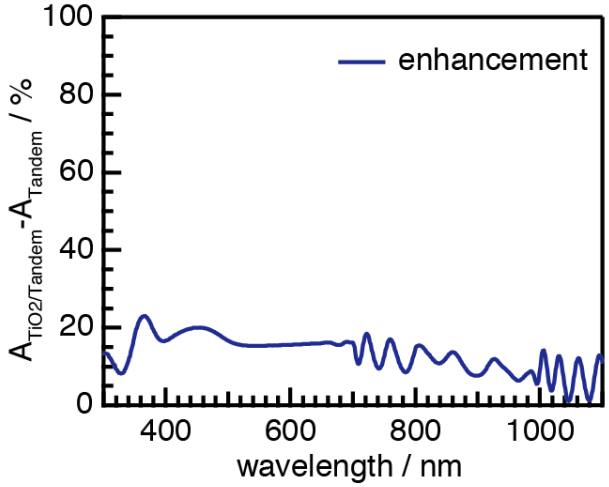

Figure S9. The enhancement of absorption based on the reduction of the reflectivity for the PEC device due to employment of TiO_2 layer. (Absorption = 1-Reflection) The 15% average increase of absorption can directly contribute to the enhancement of photocurrent.

Section S6. Optimization of the optical design

To assess the optical thickness, we performed a series of optical reflectivity measurements on TiO_2 films deposited by atomic layer deposition (ALD) on the tandem photoelectrodes with various thicknesses in the range of interest. The results are shown in Fig. S10 below, which displays the results for TiO_2 films of different thickness as compared with the original reflectivity data from our optimized device (yellow curve). We find in Fig. S10a that the 30 nm thickness TiO_2 layer reported in the manuscript has the lowest reflection in the relevant spectral range. Fig. S10b shows results of calculations using full wave electromagnetic simulations performed using finite-difference time-domain methods (Lumerical FDTD) assessing the effect of thickness variations on optical reflectivity similar to the experimental results. For the TiO_2, we find a very low reflectivity over a wide spectral range for a nominal thickness of 30 nm.

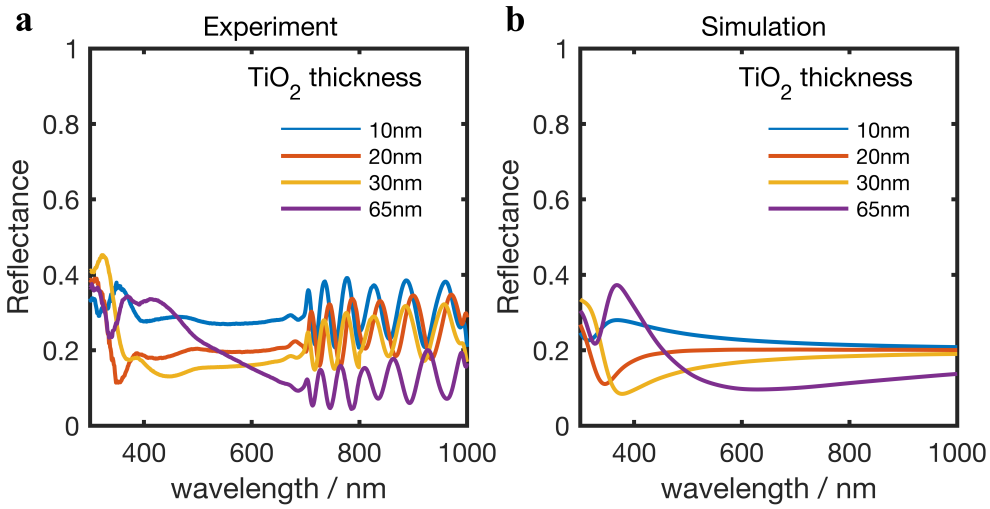

Figure S10. a) Reflectance R_a, measured in air, of the dual-junction tandem solar cell with different thicknesses of the TiO_2 coating by changing the ALD deposited cycles; (b) Reflectance R_a, simulated by Lumerical's FDTD, with different thicknesses of TiO_2 for correlation with the experimental results.

To optimize light coupling, we also carefully tailored the optical properties of the Rh nanoparticles to work in combination with an optimum TiO_2 thickness of 30 nm, determining the reflectance, absorbance and transmittance. To determine the influence of the Rh particle size on reflectance, absorbance and transmittance we modeled three particle sizes using full wave electromagnetic simulations. The optical transmission modeling in Fig. S11 shows that for a 10 nm Rh particle size, an optimum is reached. In Fig. S11b, we show that the transmittance and photoelectrode light coupling for the entire structure consisting of (tandem photoelectrode/30 nm TiO_2/10 nm Rh particles) is almost identical to a bare surface without Rh.

Although a 40 nm Rh particle size shows lower reflectivity in the relevant spectral range in Fig. S11a, the Rh particle absorption increases substantially, resulting in an overall lowered

transmittance into the cell, as seen in Fig. S11c. The transmittance is therefore reduced and fewer photons reach the photoactive part of the cell (see Fig. S11b). This trend is observed in the experimental results shown in Fig. S12. We measured the reflectance of samples with different particle size. The blue curve shows the reflectance of the tandem with a TiO_2 layer, but without Rh catalysts. The red curve shows the system with ~10 nm Rh particles added, as used in our record device. As can be seen from the simulations in Fig. S11b, we expect the 10 nm Rh particles to be effectively transparent. The yellow and purple curves show the reflectance with medium and large sized Rh particles, which would lead to a larger loss due to parasitic absorption and reflection.

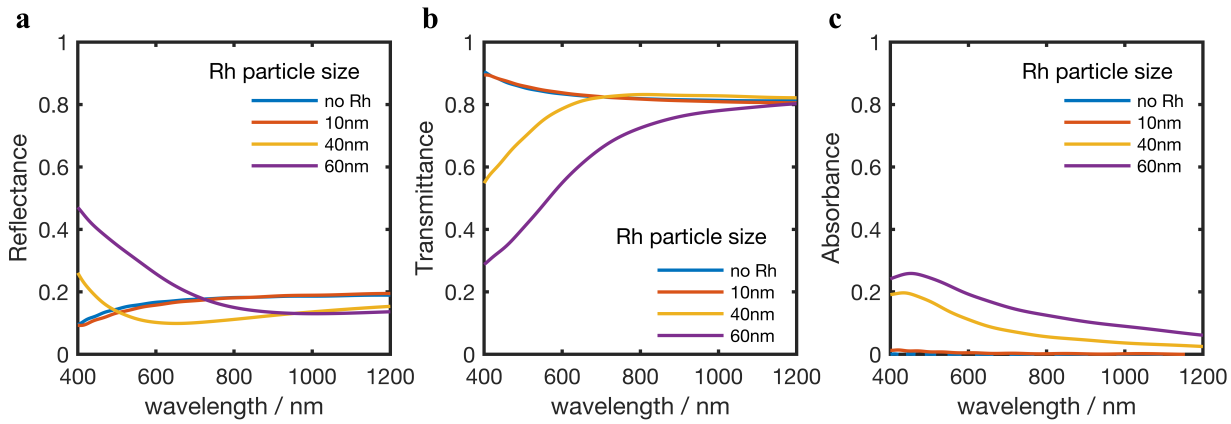

Figure S11. FDTD simulated (a) reflectance, (b) transmittance, and (c) absorption defined as A = 1 - R - T of different Rh particle sizes on 30 nmTiO_2/AlInP (window layer of the tandem).

The calculations above for Fig. S11 show that for Rh sizes greater than 20 nm, less light reaches the photoactive parts of the tandem photoelectrode. In that case, the splitting of the quasi Fermi levels will result in a reduced photovoltage and the operation point would shift to lower potentials, decreasing the STH efficiency in a non-linear manner. However, the working potentials at given current density at both electrodes (HER working electrode and OER counter electrode) will decrease as well as the solution resistance. Simulations (see Refs. [7,8]) show that this can overcompensate the loss in photovoltage. The STH then depends linearly on the light intensity via the photocurrent and drops according to eqn. 1.

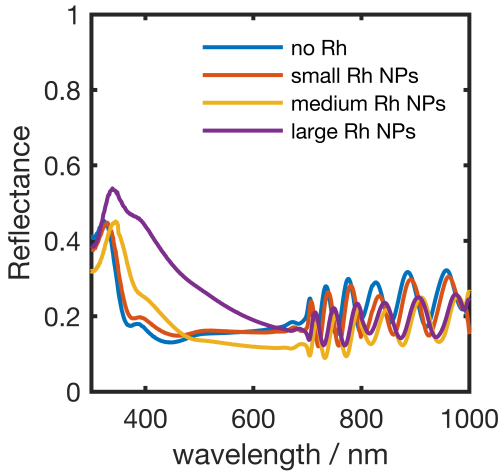

Figure S12. Reflectance R_a, measured in air, of samples with different Rh NPs size on the dual-junction tandem solar cell with 1500 ALD cycles TiO_2 corresponding to a layer thickness of 30 nm.

Section S7. Assessment of the solar-to-hydrogen efficiency measurement

Photoelectrochemical measurements

All photoelectrochemical measurements were performed using Biologic SP-200 potentiostats. 1 M $HClO_4$ was used as the electrolyte for pH 0 and 0.5 M KH_2PO_4/K_2HPO_4 phosphate buffer for pH 7. All electrolytes were purged with N_2 (4N) for minimum 1 h before usage. A saturated calomel electrode (SCE) was used as the reference electrode for three-electrode measurements.

Custom-made three-necked cell Glass cells with a quartz window with a volume of 35 mL where used as the vessel for the experiments allowing them to be easily cleaned in Aqua Regia. To avoid internal reflections in the cell, a black mask was directly attached in front of the quartz window so that only the sample itself was illuminated. The tandem device with areas ranging from $0.1 - 0.3\ cm^2$ was positioned 10 mm away from the quartz window with the counter electrode of a size of $0.6\ cm^2$ being placed in close vicinity to the working electrode. The photograph of the custom-build cell is showed in Fig. S13. The electrolyte was vigorously agitated with a magnetic stir bar to minimize the diffusion losses. J-V measurements were performed with a scan velocity of 50 mV/s. To prevent the degradation from running at anodic condition where the dark current occur, we only recorded J-V curves until 0 V vs. the counter electrode. Stability and efficiency tests were carried out in a two electrode configuration using a calibrated Class AAA AM1.5G solar spectrum provide by an ABET Technologies Sun 3000 Solar Simulator (Fig. S14). The light intensity was set to $100\ mW/cm^2$ using a calibrated silicon reference solar cell.

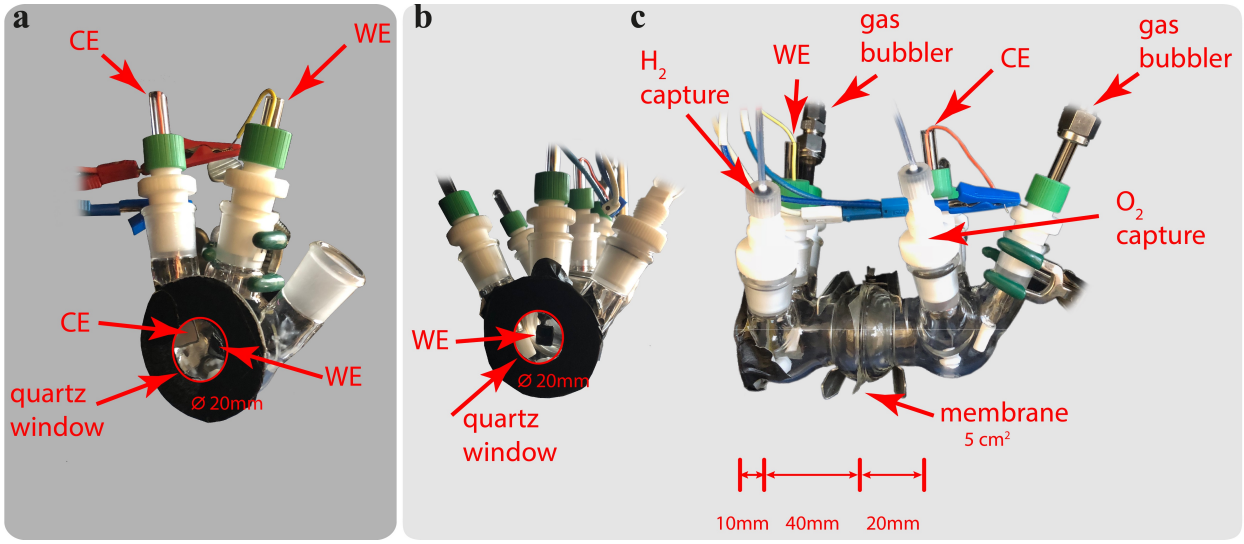

Figure S13. (a) Cell used for high efficiency benchmarking with WE and CE in close vicinity. The distance WE to window is 10 mm and the distance WE to CE is < 10 mm. (b) Front view and (c) side view of the double glass cell used for gas collection. The distance WE to window is 10 mm, the distance WE to membrane is 40 mm and the distance membrane to CE is 20 mm. The membrane has an area of 5 cm^2. Each compartment has a gas bubbler for pre-saturation of the electrolyte with H_2/O_2 purging and gas outlets which are connected to inverted water filled burette for gas collection. For both cells (a) and (b/c) the quartz window is covered with black tape having an opening with ∅ 20 mm.

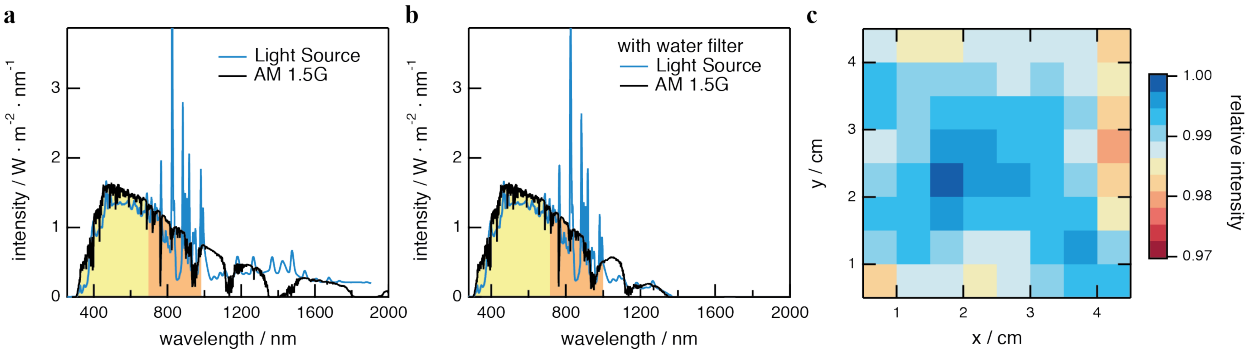

Figure S14. (a) Light spectrum of the solar simulator (ABET Sun 3000 Solar Simulator) and AM1.5G spectrum. (b) Light spectrum of the solar simulator and AM1.5G with water filter. (c) Uniformity map of the solar simulator illumination area. The band gaps of the dual-junction light absorber are indicated in (a) and (b). (yellow color for top cell and orange color for bottom cell).

Gas collection

To obtain the Faraday efficiency, hydrogen and oxygen gas collection were performed using a eudiometric gas collection setup. A SELEMINON ion exchange membrane with an area of 5 cm^2 in size was utilized to separate the cathode and anode chamber. Electrolytes were purged with ultrapure N_2 (4N), the cathode side was pre-sutured with H_2 and the anode side was pre-saturated with O_2 by means of H_2 and O_2 gas bubbling through a fine gas dispersion frit for an hour. Each side was sealed against the ambient but connected via a short thin tubing to an inverted water filled burette (purged and pre-saturated). The change in pressure in each burette upon H_2 and O_2 gas collection due to photoelectrochemical water splitting in the PEC cell was monitored by pressure transducers (EXTECH HD755). The change in pressure over time was then converted to a gas volume under consideration of the reduced pressure in the inverted burette.

For constant temperature, $\Delta V_0 = \frac{P}{P_0} \cdot \Delta V$ with $P = (407.2 - h)$ and $P_0 = 407.2$, using inWC as pressure units. $\frac{P}{P_0}$ is the volumetric correction factor necessary to account for reduced pressure in the inverted burette.

The expected produced volume of hydrogen and oxygen gas for the cathodic and anodic reaction was calculated by the transferred electrical charge as measured by the potentiostat.

Spectral correction factor and light concentration factor

In order to consider the influence of the spectral mismatch of the irradiance between our solar simulator and the AM1.5G spectrum, a spectral correction factor (SCF) was calculated. It is based on the relative EQE of the device, the irradiance of the solar simulator $\{I_{meas}(\lambda)\}$ and the AM1.5G reference spectrum $\{I_{AM1.5G}(\lambda)\}$ (Fig. S14a). The influence of the water filter $\{F_{water}(\lambda)\}$ on the spectra was considered for the calculations (Fig. S14b). The index j denotes to the individual sub cell.

$$J_{AM1.5G} = J_{meas} \cdot \frac{\min_j \int_{280nm}^{1200nm} I_{AM1.5G}(\lambda) \cdot F_{water}(\lambda) \cdot EQE_{j,device}(\lambda) d\lambda}{\min_j \int_{280nm}^{1200nm} I_{meas}(\lambda) \cdot F_{water}(\lambda) \cdot EQE_{j,device}(\lambda) d\lambda} = J_{meas} \cdot SCF \quad (1)$$

For illumination under AM1.5G conditions the AM1.5G ASTM G-173 reference spectrum was taken from the Renewable Resource Data Center (RReDC) of the National Renewable Energy Laboratory (NREL). Although the SCF is a simple correction between spectra, we still need to be careful to prevent artificial inflation or underestimation of efficiency. We note that the SCF will be unsuitable to apply with large deviation from 1 since the current correction will become unrealistic due to severe difference of overpotential and bubble formation.

To correct for nonparallel illumination in the solar simulator that results in focusing of the light by the quartz window, the beam divergence in each axis was experimentally determined and a

concentration ratio (CR) was calculated (Fig. S15). The corrected photocurrent is given by $J_0 = \frac{J_{meas}}{CR}$.

The exposed electrode surface area was precisely determined using an optical scanner and the open source software ImageJ. The steep edge of the high-viscosity epoxy was used as a borderline. Hence, the spill-out area (~20 μm, see reference [9]) was fully included in the area measurement. In this study the electrodes had different areas of 0.1 – 0.3 cm^2.

The total correction factor for each sample is then given by $J_{AM1.5G} = J_{meas} \cdot SCF/CR$, e.g. for the 19.3 % efficient cell reported in Fig. 2b and 3a, the values are SCF = 1.024 and CR = 1.028.

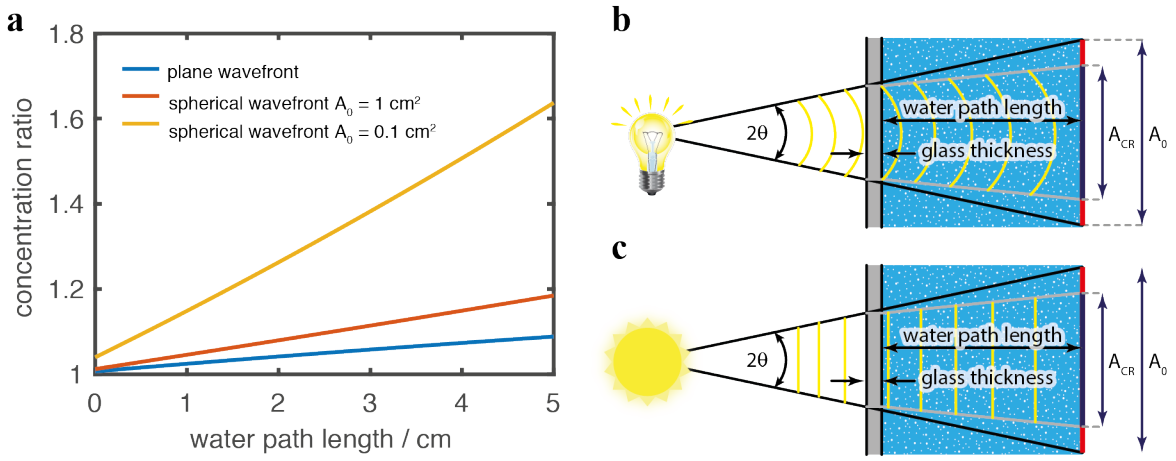

Figure S15. (a) Calculated optical concentration ratio of the non-parallel light-beam of solar simulator illumination in PEC cells for plane wavefront and spherical wavefront as a function of water path length. (b) Illustration of the spherical wavefront case. The concentration ratio ($CR = A_0/A_{CR}$) depends on the exact sample area A_0. (c) Illustration of the plane wavefront case. An opening aperture in front of the quartz window of the PEC cell with a diameter of 2 cm was used in this study. The beam divergence was experimentally determined to be $\Theta_V = 1.8$ ° vertically and $\Theta_H = 2.5$ ° horizontally by measuring the size increase of the light beam through a 2 cm aperture at specific distances (10 cm to 30 cm).

External quantum efficiency measurement

External quantum efficiency (EQE) measurements were performed on fully processed tandem devices solely to calculate the spectral correction factor to account for the difference between artificial and solar illumination. Hence, to avoid hydrogen evolution and H_2 bubble formation during EQE measurements, a 50 mM methyl viologen hydrate (98%, ACROS Organics), dissolved in ultrapure water, was used as the electrolyte. For continuous light biasing of each individual tandem sub-cell during EQE measurements of the complementary sub-cell, a 780 nm high-power LED (Thorlabs M780L2) was used to bias the bottom cell and a 455 nm high-power LED (Thorlabs M455L2) was used to bias the top cell. Monochromatic illumination was delivered by an Oriel Solar Simulator with a 150 W Mercury-Xenon arc lamp attached to a Newport monochromator (1200 lines/mm). The monochromatic light was chopped at 10 Hz. The modulated photocurrent was amplified by an SRS model SR570 low noise current preamplifier. The current preamplifier was also used to supply a -1 V bias to the tandem working electrode to ensure measurement in the light limiting current regime. A coiled Pt wire was used as the counter electrode for this two-electrode measurement.

The output from the preamplifier was then measured by a SRS model SR830 lock-in amplifier which was phase locked to the frequency of the optical chopper yielding the photocurrent for the individual sub-cell $J_{top/bottom}(\lambda)$.

To measure the absolute light intensity ($W \cdot nm^{-1} \cdot cm^{-2}$) as delivered by the monochromator, a certified calibrated silicon diode (biased at -1 V) was positioned in the light path inside the photoelectrochemical cell filled with the electrolyte (to exclude effects of the electrolyte and quartz window on the measured light intensity) and the photocurrent density was measured (the LED's for light biasing of the tandem were switched off during this reference scan). The photocurrent density could then be converted to the light intensity $I(\lambda)$ by the known spectral response of the silicon diode.

The EQE for each sub-cell is then given by equation (2).

$$EQE_{top/bottom}(\lambda) = \frac{R_{top/bottom}(\lambda)}{\lambda} \cdot \frac{hc}{e} = \frac{J_{top/bottom}(\lambda)}{I(\lambda)} \cdot \frac{1}{\lambda} \cdot \frac{hc}{e} \quad (2)$$

$J_{top/bottom}(\lambda)$ is the photocurrent density of the corresponding sub-cell in $A \cdot nm^{-1} \cdot cm^{-2}$, $I(\lambda)$ the light intensity delivered by the monochromator in $W \cdot nm^{-1} \cdot cm^{-2}$, λ is the wavelength in nm, h is the Planck constant, c is the speed of light in a vacuum, and e is the elementary charge. $R_{top/bottom}$ is the spectral response for each sub-cell.

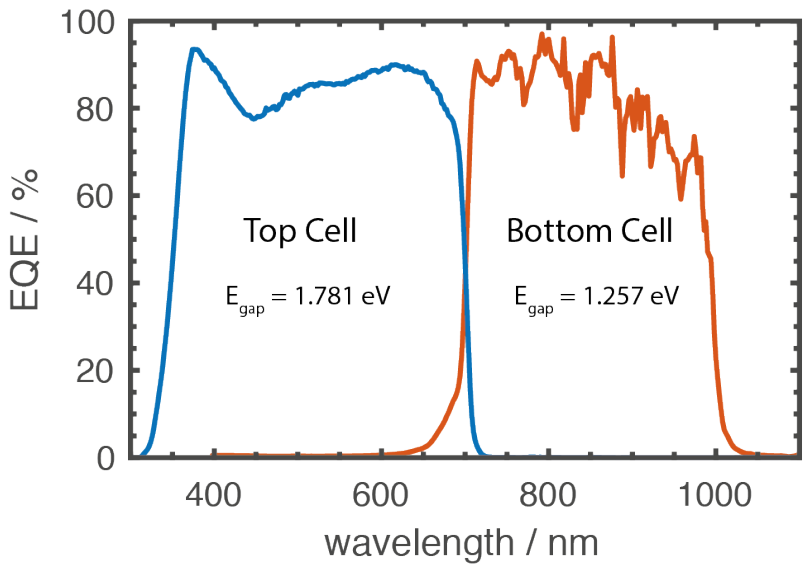

Figure S16. Relative EQE of a fully processed PEC tandem device: The bandgap combination is determined to be around 1.78 eV for the top cell and 1.26 eV for the bottom cell. To calculate the spectral correction factor (SCF) between solar simulator and the AM1.5G spectrum, the EQE measurements were performed in 50 mM methyl viologen where no bubble formation will deteriorate the accuracy. The bias light was 780 nm and 455 nm for the bottom and top sub-cell, respectively.

Polarization losses

For an evaluation of the influence of polarization losses including ohmic losses, diffusion losses and and kinetic losses [10], we simulated the maximum obtainable efficiencies in the detailed-balance scheme with the program YaSoFo [9]. Since the electrolyte was vigorously agitated and buffered, we are able to minimize the diffusion losses. Due to our findings above, optical losses (see Supplementary Section S6) were assumed to be the cause for the difference in theoretical and practically obtained limiting photocurrents. In the simulation, these were taken into account by scaling the AM 1.5G spectrum with a constant factor of 0.89. The diode current-voltage curve (ideality factor n_i=1) was intersected with the characteristics of the catalyst following a Tafel behavior described by exchange current density and Tafel slope under the assumption of an additional ohmic drop of 2 Ω. Fig. S17a shows the maximum STH efficiency as a function of exchange current density and Tafel slope. We observe that in the regime of our OER catalyst (exchange current density of ~10^{-3} mA·cm^{-2} for RuO_2, Tafel slope for RuO_2 as 83 mV·dec^{-1} at pH 0 and 100 mV·dec^{-1} at pH 7, see Fig. S3), the exchange current density and Tafel slope are still in the plateau of the maximum efficiency; the corresponding points are indicated in Fig. S17a. As in our case catalysis is dominated by the OER, it is not an efficiency-limiting factor of our setup. We also show in Fig. S17b the efficiency as a function of the ohmic drop. For this analysis, we fixed exchange current density and Tafel slope to typical values of IrO_2 and varied the ohmic resistivity. One notices that the efficiency only starts to drop at high values beyond 40 Ω, which is why the resistive overpotential is not limiting in our setup, either. Combining the ohmic loss that can be induced from the electrolyte (~4 Ω for pH 0 and ~15 Ω for pH 7), and interface loss from imperfect surface band alignment (~40 Ω without TiO_2 and ~6 Ω with TiO_2), our record device photocurrent is still located at the linear region which indicates that the optical losses are prevailing in our system.

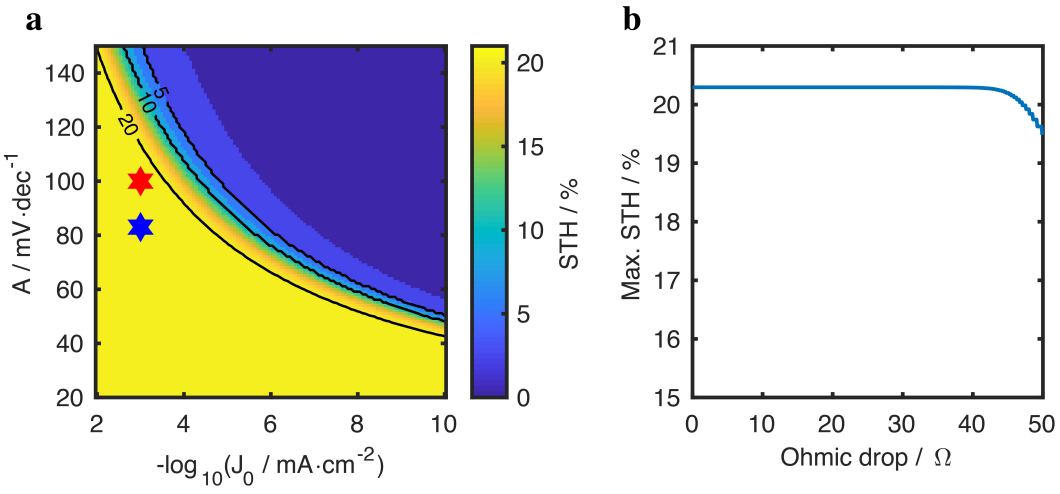

Figure S17. Calculated maximum STH efficiency as function of (a) Tafel slope A and exchange current density J_0, (b) ohmic drop. Maximum obtainable efficiencies for the given tandem absorber are shown in the detailed-balance scheme as a function of the catalyst parameters and resistivity loss. The maximum photocurrent density was scaled to the experimentally determined current density under strong cathodic bias. The blue star indicates our device under pH 0 condition and red star indicates our device under pH 7 condition.

Section S8. Comparative PEC test conditions and results

Compared to an earlier reported record photoelectrosynthetic cell with inverted metamorphic multi-junction semiconductor architecture [11], the tandem device employed in the present study has a less ideal bandgap combination of 1.78 V/1.26 V, compared to 1.8 V/1.2 V, which leads to the reduction of theoretical efficiency from 24.2 % to 22.8 %. However, due to better light management (antireflection layer, optimized catalyst loading, thinning and transparency of the tunnel junction), a higher current density and higher STH efficiency of 19.3 % are observed. This efficiency corresponds to an enhancement from 67 % to 85 % of the ratio of achieved efficiency to theoretical efficiency for the employed bandgaps. The stability tests using a two-electrode configuration at 0 V vs. RuO_2 counter electrode to demonstrate unassisted water splitting for the two devices are shown in Fig. S18. The result from [11] was corrected by scaling the initial current density (including spectral calibration errors) to 13.17 mA/cm^2 calculated from their reported highest efficiency of 16.2%. At acidic pH, our device current density drops from 15 mA/cm^2 to less than 5 mA/cm^2 within an hour. By contrast, for pH 7, the photocurrent density and device performance are more stable and show similar chronoamperometric performance to that reported in [11]; our device is stable for the first 20 min, then the photocurrent density slowly decreases. The spikes in current density indicate the influence of bubble formation and subsequent detachment. The dynamics are different due to the change in the reduction mechanism (proton reduction at pH 0, water reduction at pH 7) and the surface tension of the electrolyte. The surface tension of the phosphate buffer is higher than for acidic electrolyte (see Supplementary Section S9), and exhibits more severe bubble accumulation that induces greater photocurrent density fluctuations.

It is well known that photoelectrochemical devices can be better stabilized in a three-electrode configuration at the RHE potential. We were also able to demonstrate long-term stability of 50 hrs under these conditions without the existence of a protection layer in acidic environment (see

Fig. S19). However, these conditions are not comparable to operation at 0 V vs. CE in a two-electrode configuration, as operation at RHE potential diminishes the effect of corrosion. For comparison and to understand the intrinsic differences between operation at different pH conditions, chronoamperometric tests were conducted at -0.4 V vs. counter electrode (equivalent to approximately +1.1 V with respect to RHE (estimated to be 1.23 V plus catalysts overpotential minus 0.4 V) as shown in Fig. S20. The stability data of the device reported in [11], which was operated at +0.6 V vs. RHE with and without current rescaling, is included for comparison. It shows that the device photocurrent density decreases in acidic electrolyte to low values within 3 h. We conducted XPS measurements to further understand the degradation mechanism (Supplementary Section S10). The pristine sample before any photoelectrochemical test has full coverage of protection layer on top of window layer without pinhole; however, the Rh catalysts do not cover 100 % of the TiO_2 surface. We conclude that at pH 0, the exposed TiO_2 experiences local catalyst detachment and decomposes by chemical etching, degrading its ability to protect the underlying photoelectrode. In neutral pH electrolyte, stability over 20 h was demonstrated, with the photocurrent density remaining at 83 % of its initial value. At 12 h into the test, a diurnal cycle was simulated by emersion of the sample in the dark for a few minutes. This step resulted in a substantial current density increase, indicating that the previous reduction in current density was not mainly a result of loss of catalyst material or the corrosion of the protective layer, which are both non-reversible. Instead, we suggest that PO_x groups formed on the cathode during HER and the reaction of OH^- with the buffer may poison the catalysts and lead to the observed performance degradation (see XPS data in Supplementary Section S9). We note that the source of phosphate species was determined to be the buffer electrolyte rather than tandem corrosion since no indium signal is detected. We propose that surface-bound PO_x groups were detached during the dark recovery procedure, leading to a recovery of over 50 % of the original current density loss. The residual loss remaining after dark recovery can be attributed to the PO_x

groups still remaining on the surface. We find that at neutral pH, the protection layer remains intact, as the absence of In and P signals from the underlying AlInP window layer, and leads to the further prolonged stability. Thus overall, our device operated in neutral pH conditions show similar stability characteristics compared to that reported in [11], while exhibiting higher efficiency. Our device, operated in a biased two-electrode configuration exhibits an extended stability with respect to the three-electrode measurements reported in [11].

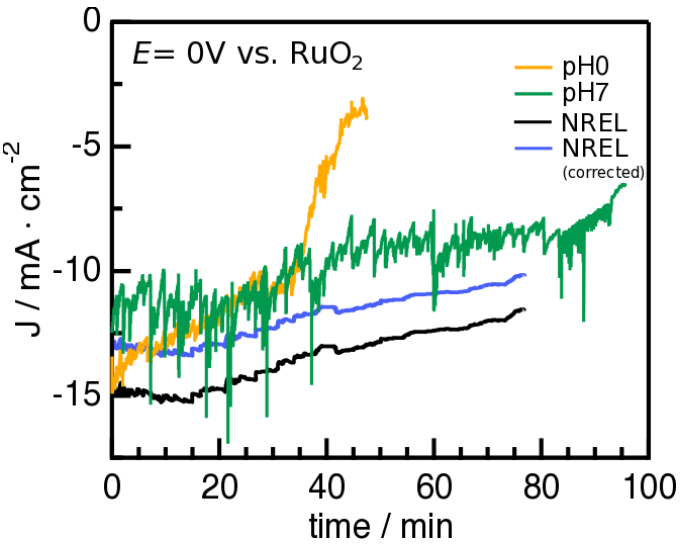

Figure S18. Stability measurements at 0 V vs. RuO_2 counter electrode for acidic and neutral pH. The result from [11] are adapted and included for comparison as the black curve, and in blue with current rescaled based on the reported efficiency in [11].

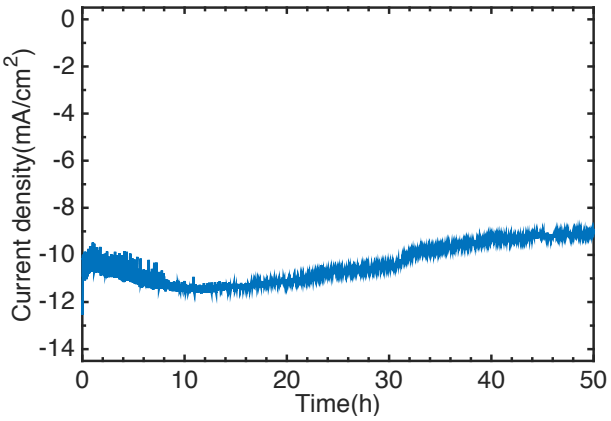

Figure S19. Chronoamperometric measurements at 0 V vs. RHE for Rh/Tandem device without protection layer in acidic environment.

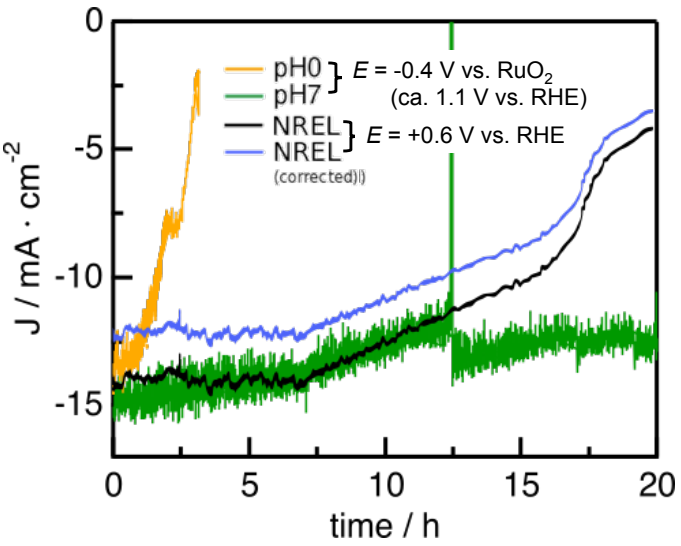

Figure S20. Chronoamperometric measurements at -0.4 V vs. RuO_2 counter electrode for acidic and neutral pH. The result from [11] at 0.6 V vs. RHE are adapted and included for comparison as in black, and in blue with current rescaled based on the reported efficiency in [11].

Section S9. Surface tension variation between pH0 and pH7

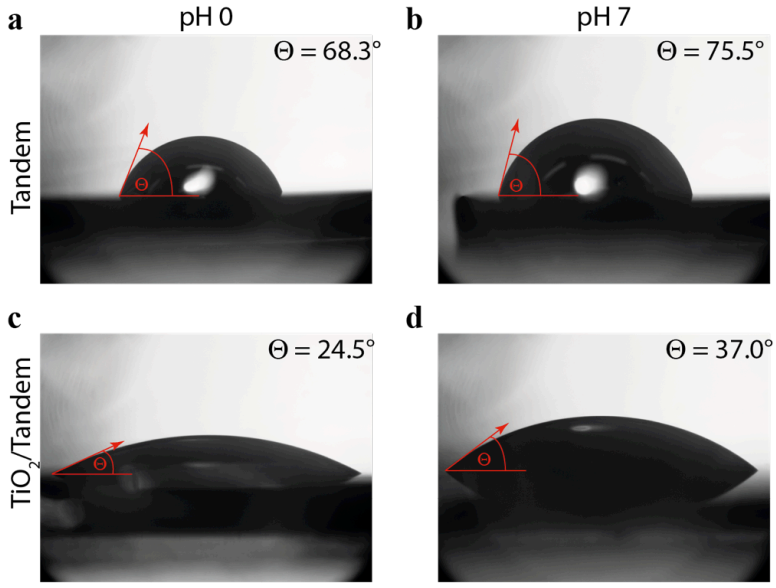

Figure S21. Contact angle measurement for pH0 1 M $HClO_4$ (a, c) or pH7 0.5 M phosphate buffer (b, d) on the tandem (a, b) or on the TiO_2/tandem (c, d) sample. The image was analyzed with ImageJ with the help of the 'Drop Analysis' plugin developed at the École polytechnique fédérale de Lausanne (EPFL) (http://bigwww.epfl.ch/demo/dropanalysis/). The larger contact angle of phosphate buffer indicates higher surface tension, which can lead to more severe bubble accumulation and larger photocurrent density fluctuations.

Section S10. X-ray photoelectron spectra and mechanism development

The XPS results are presented in the same intensity scale if not noted otherwise.

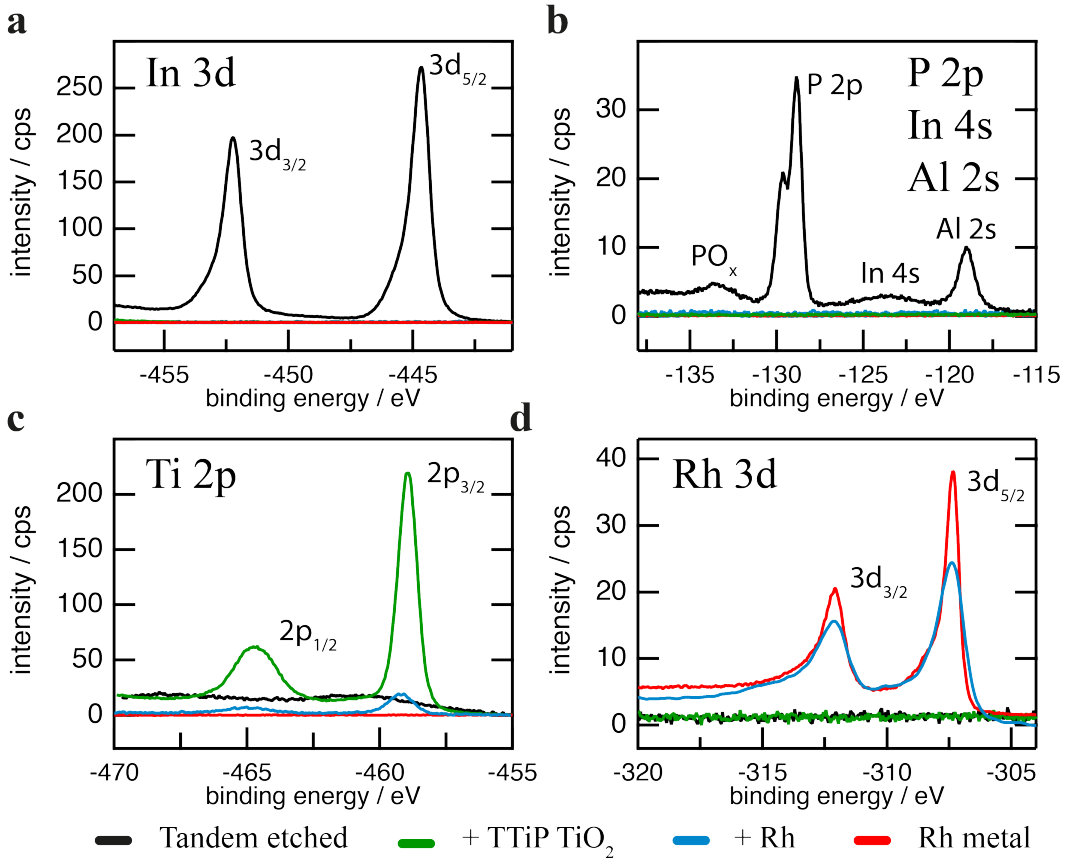

Figure S22. X-ray photoelectron spectra of tandem samples after each step in the PEC device production process: after removing the GaAs/GaInAs cap layer by chemical etching (black curve, indicated as Tandem etched), after deposition of the TiO_2 layer by ALD (green curves, indicated as +TTiP TiO_2); and after photoelectrochemical deposition of Rh nanoparticle catalysts (blue curve, indicated as +Rh). As reference, spectra of metallic Rh electrode are included (red curve, indicated as Rh metal). (a) In 3d core levels; (b) P 2p, In 4s and Al 2s core levels, the peak of PO_x is indicated; (c) Ti 2p core level; and (d) Rh 3d core level. The Tandem etched spectra show the exposed $AlInPO_x$ window layer. Upon deposition of TiO_2 with no visible In and P signal we infer full coverage of protection layer without pinhole formation. Photoelectrochemical

deposited Rh with the similar intensity to the Rh film indicates sufficient amount of catalysts. However, the small remaining Ti peaks present the existence of the TiO_2 exposed area.

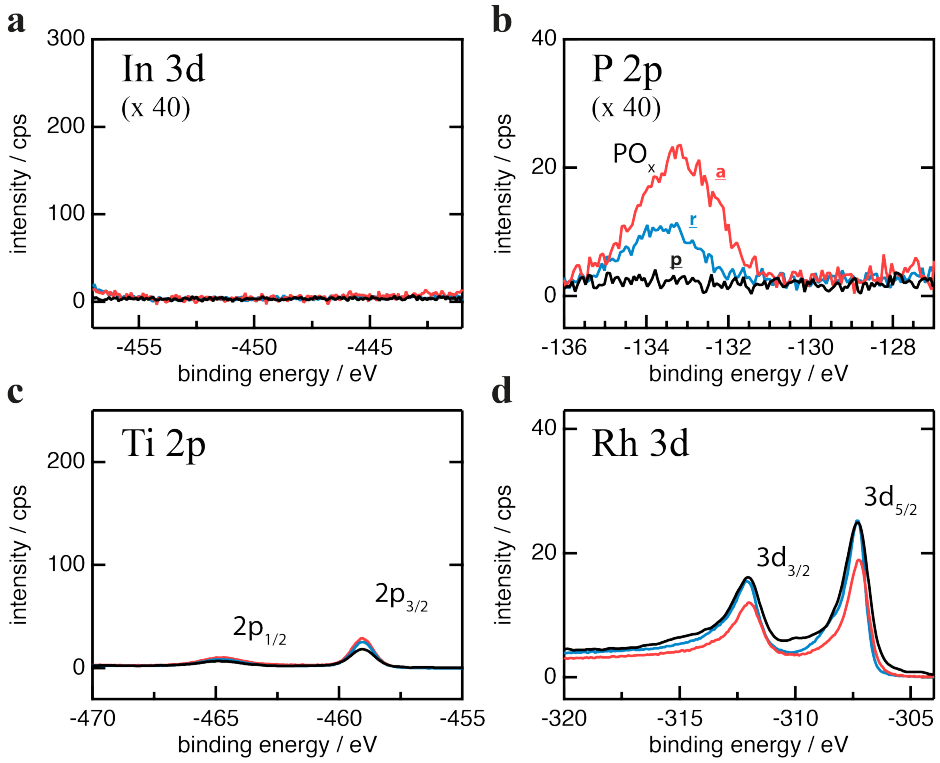

Figure S23. X-ray photoelectron spectra for the study of Rh catalyst poisoning by PO_x groups in pH 7: (a) In 3d core levels; (b) P 2p core levels, the peak of PO_x is indicated; (c) Ti 2p core level; and (d) Rh 3d core level. The black curve indicates the pristine (p) sample before any photoelectrochemical measurement. The red curve indicates the aged (a) sample, which was taken out from the electrolyte under light illumination after operation. The blue curve indicates the recovered (r) sample, which was taken out from the electrolyte under dark condition to simulate the diurnal cycle. We observed the enhancement of the phosphate peak for the aged sample and reduction again after the recovery. Note that no In signal is detected in all samples which indicates the source of phosphate species is the buffer electrolyte rather than tandem corrosion. Since the corrosion and severe catalyst detachment are both not observed in our

samples, and are impossible to lead to the degradation that is recoverable, we deduce that the current reduction during the stability test is mainly contributed by the poisoning of Rh catalysts by the phosphates group.

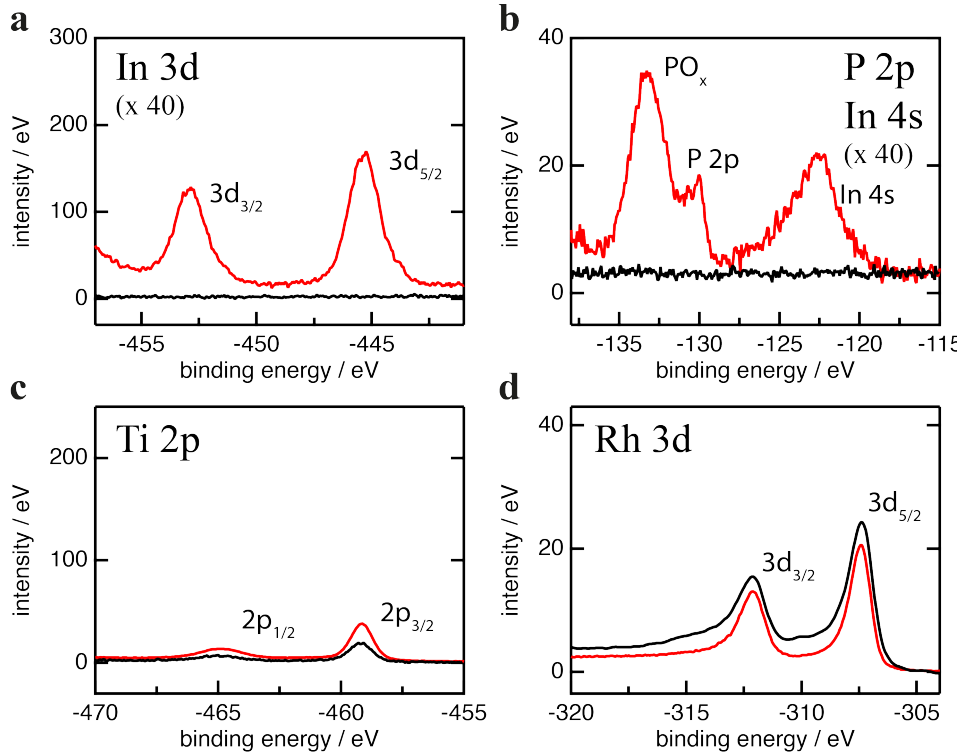

Figure S24. X-ray photoelectron spectra of a pristine Rh/TiO_2/Tandem sample (black) and after degradation in acidic environment (red): (a) In 3d core levels; (b) P 2p and In 4s core levels, the peak of PO_x is indicated; (c) Ti 2p core level; and (d) Rh 3d core level. The TiO_2 peak enhancement indicates more exposed area upon local detachment of catalysts. However, the maintained prominent Rh peak implies the loss of catalyst is not the limiting factor of degradation. Instead, the appearance of underlying In and PO_x peaks supports the scenario of tandem corrosion due to local TiO_2 etching.

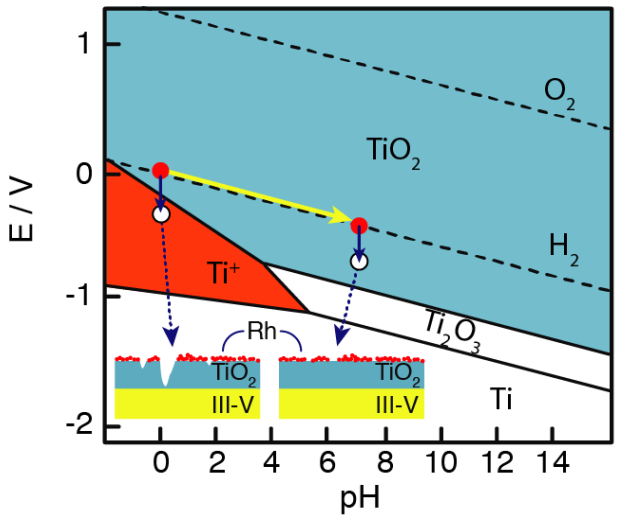

Figure S25. Potential-pH equilibrium diagram for the system titanium-water system at 25 °C, adapted from ref. [12]. For pH 0, the stable region is small. Upon overpotential to hydrogen evolution, corrosion sets in which ultimately leads to the degradation of the device and its efficiency. The pristine sample before any photoelectrochemical test has full coverage of protection layer on top of window layer without pinhole; however, the Rh catalysts do not cover 100 % of the TiO_2 surface. We conclude that at pH 0, the exposed TiO_2 experiences local catalyst detachment and decomposes by chemical etching, degrading its ability to protect the underlying photoelectrode. We find that at neutral pH, the protection layer remains intact, as the absence of In and P signals from the underlying AlInP window layer, and leads to the further prolonged stability.

Section S11. STH benchmarks

Table S1. Reported STH benchmarks from literature with employed bandgaps, achieved STH efficiency (η_{STH}), theoretical limit for realistic water splitting (η_{theo}) and ratio of achieved STH to η_{theo} as η^{*}_{theo}.

	Bandgaps	η_{STH} **/ %**	η_{theo} **/ %**	η^{*}_{theo} / %	**Reference**
JCAP/TU-I/ISE	1.78/1.26	19.3	22.8	85	This work
NREL	1.8/1.2	16.2	24.2	67	(12)
TU-I/HZB/JCAP/ISE	1.78/1.26	14	22.8	61	(15)
JCAP	1.84/1.42	10.5	19.7	53	(16)
NREL	1.83/1.42	10	19.7	51	(17), (12)

References

(1) Dimroth, F.; Beckert, R.; Meusel, M.; Schubert, U.; Bett, A. W. Metamorphic $Ga_yIn_{1-y}P/Ga_{1-x}In_xAs$ Tandem Solar Cells for Space and for Terrestrial Concentrator Applications at C > 1000 Suns. *Prog. Photovoltaics* **2001**, *9*, 165–178.

(2) Ohlmann, J.; Sanchez, J. F. M.; Lackner, D.; Förster, P.; Steiner, M.; Fallisch, A.; Dimroth, F. Recent Development in Direct Generation of Hydrogen Using Multi-Junction Solar Cells. *AIP Conf. Proc.* **2016**, *1766*, 080004.

(3) Chor, E. F.; Zhang, D.; Gong, H.; Chong, W. K.; Ong, S. Y. Electrical Characterization, Metallurgical Investigation, and Thermal Stability Studies of (Pd, Ti, Au)-Based Ohmic Contacts. *J. Appl. Phys.* **2000**, *87*, 2437.

(4) Hu, S.; Shaner, M. R.; Beardslee, J. A.; Lichterman, M. F.; Brunschwig, B. S.; Lewis, N. S. Amorphous TiO2 Coatings Stabilize Si, GaAs, and GaP Photoanodes for Efficient Water Oxidation. *Science* **2014**, *344*, 1005–1009.

(5) Bae, D.; Pedersen, T.; Seger, B.; Iandolo, B.; Hansen, O.; Vesborg, P. C. K.; Chorkendorff, I. Carrier-Selective P- and N-Contacts for Efficient and Stable Photocatalytic Water Reduction. *Catal. Today* **2017**, *290*, 59–64.

(6) Rossi, R. C.; Lewis, N. S. Investigation of the Size-Scaling Behavior of Spatially Nonuniform Barrier Height Contacts to Semiconductor Surfaces Using Ordered Nanometer-Scale Nickel Arrays on Silicon Electrodes. *J. Phys. Chem. B* **2001**, *105*, 12303–12318.

(7) Fountaine, K. T.; Lewerenz, H. J.; Atwater, H. A. Interplay of Light Transmission and Catalytic Exchange Current in Photoelectrochemical Systems. *Appl Phys Lett* **2014**, *105*, 173901.

(8) Fountaine, K. T.; Lewerenz, H. J.; Atwater, H. A. Efficiency Limits for Photoelectrochemical Water-Splitting. *Nat. Commun.* **2016**, *7*, 13706.

(9) May, M. M.; Lackner, D.; Ohlmann, J.; Dimroth, F.; van de Krol, R.; Hannappel, T.; Schwarzburg, K. On the Benchmarking of Multi-Junction Photoelectrochemical Fuel Generating Devices. *Sustainable Energy Fuels* **2017**, *1*, 492–503.

(10) Singh, M. R.; Clark, E. L.; Bell, A. T. Effects of Electrolyte, Catalyst, and Membrane Composition and Operating Conditions on the Performance of Solar-Driven Electrochemical Reduction of Carbon Dioxide. *Phys. Chem. Chem. Phys.* **2015**, *17*, 18924–18936.

(11) Young, J. L.; Steiner, M. A.; Döscher, H.; France, R. M.; Turner, J. A.; Deutsch, T. G. Direct Solar-to-Hydrogen Conversion via Inverted Metamorphic Multi-Junction Semiconductor Architectures. *Nature Energy* **2017**, *2*, 17028.

(12) Pourbaix, M. *Atlas of Electrochemical Equilibria in Aqueous Solutions*; 2nd ed.; National Association of Corrosion Engineers: Houston, 1974.

(13) May, M. M.; Lewerenz, H. J.; Lackner, D.; Dimroth, F.; Hannappel, T. Efficient Direct Solar-to-Hydrogen Conversion by in Situ Interface Transformation of a Tandem Structure. *Nat. Commun.* **2015**, *6*, 8286.

(14) Verlage, E.; Hu, S.; Liu, R.; Jones, R. J. R.; Sun, K.; Xiang, C.; Lewis, N. S.; Atwater, H. A. A Monolithically Integrated, Intrinsically Safe, 10% Efficient, Solar-Driven Water-Splitting System Based on Active, Stable Earth-Abundant Electrocatalysts in Conjunction with Tandem III–v Light Absorbers Protected by Amorphous TiO_2 Films. *Energ. Environ. Sci.* **2015**, *8*, 3166–3172.

(15) Khaselev, O.; Turner, J. A. A Monolithic Photovoltaic-Photoelectrochemical Device for Hydrogen Production via Water Splitting. *Science* **1998**, *280*, 425–427.